Study of fission dynamics with a three-dimensional Langevin approach

Li-Le Liu (刘丽乐),[1,*] Xi-Zhen Wu (吴锡真),[1,†] Yong-Jing Chen (陈永静),[1] Cai-Wan Shen (沈彩万),[2] Zhu-Xia Li (李祝霞),[1] and Zhi-Gang Ge (葛智刚)[1]

[1]*China Institute of Atomic Energy, Beijing 102413, China*

[2]*Huzhou University, Huzhou 313000, China*

(Received 3 January 2019; revised manuscript received 21 March 2019; published 30 April 2019)

The three-dimensional Langevin model plus a constraint on the heavy fragment deformation is used to study the fission dynamics for uranium and plutonium isotopes at low excitation energies. The potential energy surface is calculated with the macroscopic-microscopic model based on the two-center shell model. The Werner-Wheeler approximation is used to calculate the inertia tensor and the wall-and-window model is applied to calculate the friction tensor. In this work, the influence of the model parameters on the fission fragment mass distribution is investigated. The fission fragment mass distributions for ^{234,236,239}U and ^{240}Pu at low excitation energies are calculated and compared with the results of GEF code as well as the evaluated data of ENDF/B-VIII.0. A nice agreement is found in the comparison, in which the incorporation of the constraint on the heavy fragment deformation plays an important role. In addition, the dependence of the mass distribution on the excitation energies for $n + ^{235}$U fission is also studied within the model. Furthermore, the correlation between the elongation and mass asymmetry at the scission point and the correlations of the fission time with both the elongation and mass asymmetry are studied. This study may shed light on understanding the dynamics of the superlong channel for symmetric fission and the standard channels for asymmetric fission in the GEF model and other phenomenological fission models.

DOI: 10.1103/PhysRevC.99.044614

I. INTRODUCTION

Nuclear fission is one of the most important discoveries of the 20th century, but the process of nuclear fission, involving large-scale collective motion and producing hundreds of isotopes characterized by different mass yields and kinetic energies, remains a challenge to be fully understood in its mechanism and its phenomena. Nevertheless, great progress has been made in recent years, both microscopically and macroscopically [1–11], based on the great achievement in the research of nuclear theory and experiment and the development of computational power.

The macroscopic-microscopic model has been widely used in the calculations of the nuclear masses at the ground state and fission potential energy surface (PES) [12–14], and has enabled great successes. The fission process can be viewed as the motion of a Brownian particle walking on the multidimensional potential energy surface. Randrup, Möller, *et al.* [4,15] adopted the method of random walks on a five-dimensional PES to calculate the fission fragment mass distributions, which were in remarkable agreement with the experimental data. Pomorski *et al.* [16] calculated the mass distributions by weighting the adiabatic density distribution in the collective space with the neck-dependent fission probability based on the three-dimensional PES. Furthermore, the Langevin model [17–23] has been applied by several groups to study nuclear fission and fusion reactions at higher excitation energies for more than two decades. Recently, the Langevin model has been successfully used to study nuclear fission at low excitation energies. The mass distributions and total kinetic distributions of fission fragments for some isotopes at low excitation energies were calculated with the three- and four-dimensional Langevin approach [5–7,9,24]. Sierk [8] made systematic studies of the fragment mass and kinetic energy distributions at low excitation energies as well as spontaneous fission for some uranium and plutonium isotopes with the five-dimensional Langevin approach. However, owing to the extremely complicated fission process in heavy nuclei, the fission dynamics, especially its way towards the scission point and the features and configuration of the scission point, are still far from being completely understood. Knowledge about the fission time and the correlation of the fission time to the elongation as well as the mass asymmetry at the scission point is significantly lacking [25].

In this work, the macroscopic-microscopic model based on the two-center shell model [26] and three-dimensional Langevin model plus a constraint on the heavy fragment deformation are applied to study the fragment mass distributions and kinetic energy distributions. In addition, the correlation between the elongation and mass asymmetry at the scission point is studied, which can provide us with information on the configuration at the scission point. Moreover, the fission time and its correlation to the mass asymmetry and the elongation are also investigated, which is very important for understanding the fission dynamics. The constraint on the deformation of heavy fragments is introduced, which is inspired by the

*liulile401@163.com

†lizwux9@ciae.ac.cn

real-time microscopic study of fission by Bulgac *et al.* [1], where it is clearly shown that the heavy fragments are much closer to a spherical shape compared with light fragments at very early time. Phenomenologically, it is also known that the peak of the heavy fragments in the fission fragment mass distribution almost does not change with the mass of fissioning nuclei of actinide nuclei due to the shell effect around the shell closure $N = 82$, which corresponds to a spherical shape. The Werner-Wheeler approximation [27] is used to calculate the inertia tensor, and the one-body wall-and-window model [28,29] is applied to calculate the friction tensor.

This paper is organized as follows. A detailed introduction of the model is presented in Sec. II. The results for the fragment mass distributions, total kinetic energy distribution, and fission time as well as some discussions concerning the results are given in Sec. III. In Sec. IV, a summary of the present work and future prospects are presented.

II. METHODS

A. The macroscopic-microscopic model

In the present work, the potential energy surface is calculated with macroscopic-microscopic model, where the smooth trends of nuclear potential energy are calculated with a macroscopic model and the local fluctuations such as shell effects and pairing effects are calculated with a microscopic model. The macroscopic potential energy is the sum of the deformation-dependent surface energy and Coulomb energy, which are calculated with the finite range liquid drop model [30,31]. For the microscopic correction energy, we calculate the shell correction using the Strutinsky method [32] and the pairing correction using the BCS method [33,34].

The total potential energy within the model is the sum of the macroscopic energy and microscopic energy for the same nuclear shape. The realistic description of nuclear shape during the fission process is also very important. In order to simplify the calculation, the nuclear shape is usually assumed to be axially symmetric along the z direction.

In this work, the two-center shell model (TCSM) [26] is used to calculate the levels of a single particle and the shape of nuclear surface under the assumption of volume conservation, where the nuclear surface is an equipotential surface retaining the same potential and enclosing the same volume throughout nuclear fission. The Hamiltonian of the model in cylinder coordinates is

$$H = -\frac{\hbar^2\nabla^2}{2m_0} + V(\rho, z) + V_{LS}(\vec{r}, \vec{l}, \vec{s}) + V_{L^2}(\vec{r}, \vec{l}), \quad (1)$$

where $V(\rho, z)$ is the momentum-independent part of the potential and is expressed as

$$V(\rho,z) = \begin{cases} \frac{1}{2}m_0\omega_{z1}^2 z_1'^2 + \frac{1}{2}m_0\omega_{\rho1}^2\rho^2, & z < z_1, \\ \frac{1}{2}m_0\omega_{z1}^2 z_1'^2\left(1 + c_1 z_1' + d_1 z_1'^2\right) + \frac{1}{2}m_0\omega_{\rho1}^2\rho^2\left(1 + g_1 z_1'^2\right), & z_1 < z < 0, \\ \frac{1}{2}m_0\omega_{z2}^2 z_2'^2\left(1 + c_2 z_2' + d_2 z_2'^2\right) + \frac{1}{2}m_0\omega_{\rho2}^2\rho^2\left(1 + g_2 z_2'^2\right), & 0 < z < z_2, \\ \frac{1}{2}m_0\omega_{z2}^2 z_2'^2 + \frac{1}{2}m_0\omega_{\rho2}^2\rho^2, & z > z_2, \end{cases} \quad (2)$$

with $z_i' = z - z_i$, $i = 1, 2$. z_1 and z_2 denote the positions of the centers of the left part and the right part, separated by $z = 0$. In the above formula, there are totally 12 shape parameters which could be expressed by five free shape parameters by imposing the following conditions: the potential and its derivative with respect to z are continuous at $z = 0$, $z = z_1$, and $z = z_2$; the volume of the compound nucleus must be constant during the fission process. Thus, the five free shape parameters are $\{Z_0, \delta_1, \delta_2, \eta, \epsilon\}$, defined as follows: The elongation parameter Z_0 denotes the distance between two centers, i.e., $Z_0 = z_2 - z_1$, and the fragment deformation parameter δ_i is defined by $\delta_i = (3\beta_i - 3)/(1 + 2\beta_i)$, $\beta_i = a_i/b_i$, $i = 1, 2$. The mass asymmetry is defined by $\eta = (V_2 - V_1)/(V_2 + V_1) = (A_{f2} - A_{f1})/(A_{f2} + A_{f1})$, where V_i denotes the volume of the left or right part separated by $z = 0$ and A_{fi} is the corresponding mass number of the two parts. The neck parameter ϵ is the ratio of the height of the actual potential to the deformed oscillator potential along the symmetry axis at $z = 0$, i.e., $\epsilon = \frac{E}{E'} = (1 + cz' + dz'^2)$ as shown in Fig. 1.

In this work, the potential energy is dependent on the nuclear temperature as it was given in Ref. [35],

$$V(q, T) = V_{\rm mac}(q) + V_{\rm mic}(q, T = 0)\phi(T),$$
$$\phi(T) = \exp(-a_n T^2/E_d), \quad (3)$$

where a_n is the level density parameter of the compound nucleus and E_d is the damping parameter of the shell correction and pairing correction. It is assumed that the liquid drop energy is independent of the temperature at low excitation energy and the angular momentum is small for nuclear fission induced by neutrons at low energy, so that it is negligible in this work.

In the present work, we take the heavy fragment deformation $\delta_H = 0.02$ except for those heavy fragments in the area near symmetric fission (which are away from the $N = 82$ shell closure), for which we take $\delta_1 = \delta_2 = \delta$ as the general case. The fragment mass and the kinetic energy distribution are mainly determined by the process from the saddle point to the scission point, so the appropriate neck parameter ϵ during this process is more important. In this work, the neck parameter is fixed as 0.35 which was suggested by Ref. [36]. Thus, we have three free shape parameters $\{Z_0/R_0, \delta, \eta\}$ in order to save computation time, where R_0 denotes the radius of the spherical compound nucleus and Z_0/R_0 is dimensionless like the other two shape parameters δ and η.

B. The Langevin model

The dynamical process of nuclear fission is described by the Langevin model, where the slow evolution of the nuclear

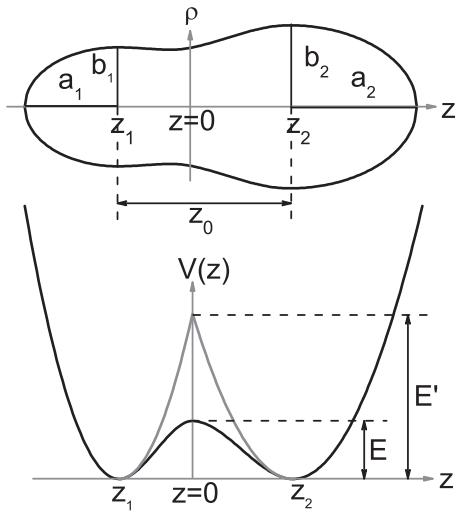

FIG. 1. The top is the nuclear shape described in the two-center shell model. The shapes of the parts on the left of z_1 and right of z_2 are semi-ellipsoid, where a_i and b_i are the semi-axes. The bottom is the corresponding actual potential and the deformed oscillator potential along the symmetry axis z.

shape is treated as the motion of a Brownian particle and the faster motion of the inner nucleons as the heating bath. The multidimensional Langevin equation describing the evolution of the collective coordinates and their conjugate momenta reads

$$\frac{dq_i}{dt} = (m^{-1})_{ij}p_j,$$
$$\frac{dp_i}{dt} = -\frac{\partial V}{\partial q_i} - \frac{1}{2}\frac{\partial (m^{-1})_{jk}}{\partial q_i}p_j p_k - \gamma_{ij}(m^{-1})_{jk}p_k + g_{ij}\Gamma_j(t), \tag{4}$$

where $q_i = Z_0/R_0, \delta, \eta$ respectively and p_i is the generalized momentum conjugate to q_i. Here in Eq. (4) and in the following equations the summation convention for repeated indices is taken. For the term of the conservative force, the free energy $F = V - a_n T^2$ should be adopted in principle; however, the contribution of the second term of free energy F vanishes if the level density parameter a_n does not depend on q_i. In this work, a_n is taken to be a constant, the same as in most of the macroscopic-microscopic model calculations that have been done. The $(m^{-1})_{ij}$ is the inverse of the inertia tensor. γ_{ij} denotes the friction tensor and g_{ij} is the strength of the random force. According to the fluctuation-dissipation theorem, g_{ij} is related to γ_{ij} by

$$g_{ik}g_{jk} = \gamma_{ij}T^*. \tag{5}$$

T^* is the effective nuclear temperature, which is usually used at low excitation energy. The correlation between T^* and general nuclear temperature T [37] is

$$T^* = \frac{\hbar\varpi}{2}\coth\frac{\hbar\varpi}{2T}. \tag{6}$$

The minimum value of $\hbar\varpi$ is given by the zero point energy, and we adopt the value $\hbar\varpi = 2$ MeV suggested in Ref. [9]. The local temperature T is usually calculated according to the equation $E_{\rm int} = a_n T^2$ based on the Fermi gas model and $E_{\rm int}$ is the intrinsic excitation energy of the compound nucleus:

$$E_{\rm int}(q) = E^* - \tfrac{1}{2}(m^{-1})_{ij}p_i p_j - V(q, T = 0). \tag{7}$$

E^* denotes the excitation energy at the initial state, which is the sum of the incident neutron energy and the binding energy.

The normalized random force $\Gamma_i(t)$ is simply assumed to be white noise:

$$\langle\Gamma_i(t)\rangle = 0, \quad \langle\Gamma_i(t_1)\Gamma_j(t_2)\rangle = 2\delta_{ij}\delta(t_1 - t_2). \tag{8}$$

In the Langevin model, the fission events are determined by identifying the different trajectories in the collective coordinate space. The Langevin equation is solved by the second-order Runge-Kutta numerical method and a Gaussian random number is used for the simulation of the random force in this work. For each trajectory, the generalized coordinates and momenta at the time $t = n\Delta t$ can be calculated when an initial condition is given. Δt is the time step, which is taken to be 0.9 fm/c. The initial condition in principle should be taken at the ground state $\{Z_0/R_0 = 0.0,\ \delta = 0.2,\ \eta = 0.0\}$. However, the fissioning rate is very low and the computation time increases hugely. In order to save the computation time, we take the initial condition at the first saddle point $\{Z_0/R_0 = 0.5,\ \delta = 0.2,\ \eta = 0.0\}$ on the potential energy surface. The initial momenta are assumed to vanish. The comparison of the results calculated with different initial conditions is made for ^{236}U fission, which will be shown in the result section. The calculation of each trajectory is terminated if it arrives at the scission point or reaches the boundaries of the generalized coordinates. The scission point is supposed to be reached when the neck radius of the compound nucleus is less than 0.5 fm in this work, which, however, will bring certain uncertainties into the fragment mass distribution and other observables. We will check the influence of the neck radius at the scission point on the fragment mass distribution, and we find that the influence is weak within the proper range.

C. The inertia and friction tensor

In this work, we calculate the inertia and friction tensor with the macroscopic approach, where the nucleus is assumed to be an incompressible and irrotational liquid drop, which has been widely used in macroscopic-microscopic model calculations [6,8,23,38,39].

The inertia tensor is calculated within the Werner-Wheeler approximation [27]. Thus, the inertia tensor is usually expressed as the following form:

$$m_{ij}(q) = \pi\rho_m\int_{z_{\rm min}}^{z_{\rm max}}\rho_s^2(z,q)\left[A_iA_j + \frac{1}{8}\rho_s^2(z,q)A_i'A_j'\right]dz, \tag{9}$$

$$A_i = \frac{1}{\rho_s^2(z,q)}\frac{\partial}{\partial q_i}\int_z^{z_{\rm max}}\rho_s^2(z',q)dz', \tag{10}$$

where ρ_m is the mass density, $\rho_s^2(z,q)$ is the value of ρ on the nuclear surface at the position z, and A_i' is the differentiation of A_i with respect to z. A_i in Eq. (10) is applied for the right part of the midplane of the nuclear shape and a similar equation

is applied for the left part, where the integration is from $z_{\min}$ to z.

The one-body wall-and-window model [28,29,40] is applied to calculate the friction tensor. For compact nuclear shapes without necks, the one-body energy dissipation mainly arises from the collision of the inner nucleons with the surface of the nuclear potential, i.e., the "wall." The wall friction tensor is written as follows:

$$\gamma_{ij}^{\text{Wall}}(q) = \frac{1}{2}\pi\rho_m\overline{\upsilon}\int_{z_{\min}}^{z_{\max}} dz \frac{\partial\rho_s^2}{\partial q_i}\frac{\partial\rho_s^2}{\partial q_j}\left[\rho_s^2 + \frac{1}{4}\left(\frac{\partial\rho_s^2}{\partial z}\right)^2\right]^{-1/2}, \tag{11}$$

where $\overline{\upsilon}$ is the average velocity of nucleons inside the nucleus, which is related to the Fermi velocity as $\overline{\upsilon} = \frac{3}{4}\upsilon_f$.

When the nuclear shape deforms strongly and the neck can be identified, the nucleons and momenta can exchange between the two prefragments, and the average velocity of nucleons in each of the two future fragments will be changed. The friction tensor then becomes

$$\gamma_{ij}^{W+W}(q) = \gamma_{ij}^{\text{Wall2}} + \gamma_{ij}^{\text{Window}}, \tag{12}$$

where

$$\gamma_{ij}^{\text{Wall2}}(q) = \frac{1}{2}\pi\rho_m\overline{\upsilon}\left(\int_{z_{\min}}^{z_N} I_L(z)dz + \int_{z_N}^{z_{\max}} I_R(z)dz\right), \tag{13}$$

with

$$I_\nu = \left(\frac{\partial\rho_s^2}{\partial q_i} + \frac{\partial\rho_s^2}{\partial z}\frac{\partial D_\nu}{\partial q_i}\right)\left(\frac{\partial\rho_s^2}{\partial q_j} + \frac{\partial\rho_s^2}{\partial z}\frac{\partial D_\nu}{\partial q_j}\right) \times\left[\rho_s^2 + \frac{1}{4}\left(\frac{\partial\rho_s^2}{\partial z}\right)^2\right]^{-\frac{1}{2}}, \tag{14}$$

where, $\nu = L, R$. z_N is the position of the smallest neck radius, which is at $z = 0$ before scission in the shape parametrization of TCSM [26]. D_L and D_R are the positions of the centers of mass of prefragments, and

$$\gamma_{ij}^{\text{Window}}(q) = \frac{\rho_m\overline{\upsilon}}{2}\left(\frac{\partial R_{12}}{\partial q_i}\frac{\partial R_{12}}{\partial q_j}\Delta\sigma + \frac{32}{9}\frac{1}{\Delta\sigma}\frac{\partial V_R}{\partial q_i}\frac{\partial V_R}{\partial q_j}\right), \tag{15}$$

where $\Delta\sigma$ is the area of the window between two parts at $z = 0$. R_{12} denotes the distance between the centers of mass of the left and right parts, and V_R is the volume on the right side of the window. The second term in Eq. (15) describes the energy dissipation arising from a change of the mass asymmetry.

During the whole fission process, a smooth transition between the pure wall friction for shapes without necks and the wall-and-window model suggested by Nix and Sierk [41] is

$$\gamma_{ij} = \tau\left(\gamma_{ij}^{W+W}\right) + (1-\tau)\gamma_{ij}^{\text{Wall}}, \tag{16}$$

where

$$\tau = \cos^2\left(\frac{\pi}{2}\frac{r_N^2}{b^2}\right), \quad b = \min(b_1, b_2), \tag{17}$$

where r_N is the radius of the neck and b is the smaller of the transverse semi-axes of the two ends.

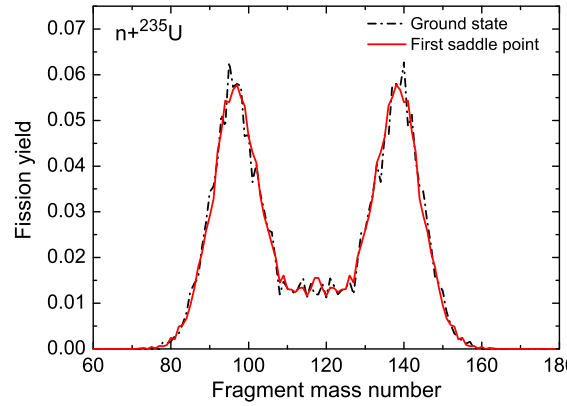

FIG. 2. The fragment mass distributions in 14 MeV $n + {}^{235}$U fission which are calculated at the initial conditions of the ground state and the first saddle point.

III. CALCULATION RESULTS

In the dynamical calculation, the potential energy V, the inverse of inertial tensor m_{ij}^{-1}, and friction tensor γ_{ij} at each time step are obtained by the parabola interpolation based on the prepared meshes in order to save computation time. These mesh values for Z_0/R_0, δ, and η are

$$Z_0/R_0 = -0.3(0.02)2.98,$$
$$\delta = -0.45(0.03)0.81,$$
$$\eta = -0.61(0.02)0.61.$$

The numbers in the parentheses are the mesh steps for each variable, and the total number of the grids is 439 890. The number of Langevin trajectories is 2.5×10^5 per fission nucleus when the initial condition is taken to be at the first saddle point and 2.0×10^6 per fission nucleus when the initial condition is taken to be at the ground state. The time step is 0.9 fm/c.

A. Influence of the initial condition, the neck radius at scission point, the shell damping parameter, and level density parameter on the fragment mass distribution

In this section, we investigate the influence of the initial condition, the neck radius at the scission point, the shell damping parameter, and the level density parameter on the fragment mass distribution, taking the case of 14 MeV $n + {}^{235}$U fission as example. Figure 2 shows the results with initial conditions taken to be at the ground state and the first saddle point. It can be found that the difference between two calculated results is almost invisible. It implies that the fission fragment distributions mainly depends on the process from the saddle point to the scission point. The result calculated from the ground state shows stronger fluctuation because of not enough fission events. Therefore, in the following, fragment mass distributions are calculated with the initial condition taken to be at the first saddle point. The scission point, i.e., the terminating point of the Langevin trajectory, is determined by a fixed neck radius, which should be comparable with a nucleon size on one hand and small enough on the other

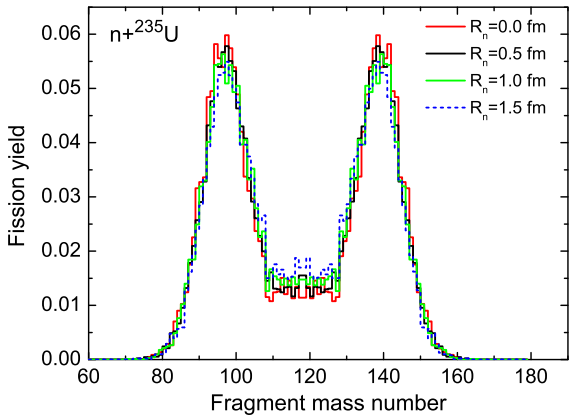

FIG. 3. The fragment mass distributions in 14 MeV $n + {}^{235}$U fission which are calculated for different values of the neck radius at the scission point.

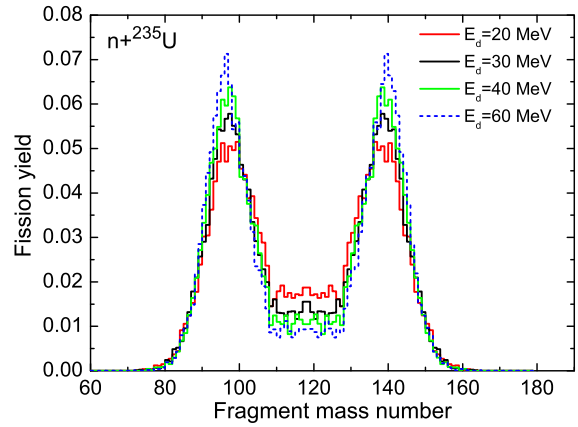

FIG. 5. The fragment mass distributions in 14 MeV $n + {}^{235}$U fission for different values of shell damping parameter E_d.

hand. The influence of the different values of the fixed neck radius for setting the scission point on the fragment mass distributions is shown in Fig. 3, which shows that with the larger fixed neck radius, the yields at the valley region will increase slightly, and the mass distributions are almost the same when the fixed neck radius for setting the scission point is in the range of 0.0–0.5 fm, which means that there is almost no exchange of nucleons between two pre-fragments on the way to the complete separation in this case. Therefore, the neck radius 0.5 fm is used to determine the scission point in this work.

The influence of the level density and the shell damping parameter on the fragment mass distributions are also investigated, and are shown in Figs. 4 and 5, respectively. It can be seen from Fig. 4 that the results calculated by different values of level density parameter change very little, which means that the fragment mass distributions are insensitive to the level density parameter. The shell damping parameter E_d in Eq. (3) has a strong effect on the ratio of the contribution of the asymmetric fission to the symmetric fission, as shown in Fig. 5. With the larger value of the shell damping parameter E_d, the damping of shell correction energy becomes weaker, which results in more events of asymmetric fission, so the fragment yields at the peak region of the mass distribution become higher and those at the valley region become lower. In the following calculations for different fissioning systems, we use the value $A_{CN}/10$ MeV^{-1} for level density parameter a_n and 30 MeV for the shell damping parameter E_d. In addition, the use of Werner-Wheeler approximation for the calculation of the inertia tensor is a strong assumption which does not consider the shell effects, while the potential energy surface contains the shell effects. Therefore, we have simply performed calculations with the inertia tensor multiplied by a factor of 0.5, 5.0, and 10.0, to check the sensitivity of the fragment mass distributions against the values of the inertia tensor. Figure 6 shows the influence of the values of the inertia tensor on the fragment mass distributions. One can find from the figure that the strength of the inertia tensor has not much obvious influence on the fragment mass distribution.

B. The fragment mass distributions for different systems

The fission fragment mass distributions in 14 MeV $n + {}^{233,235,238}$U and ^{239}Pu are calculated. In the present work, we have not taken the neutron emission into account in the

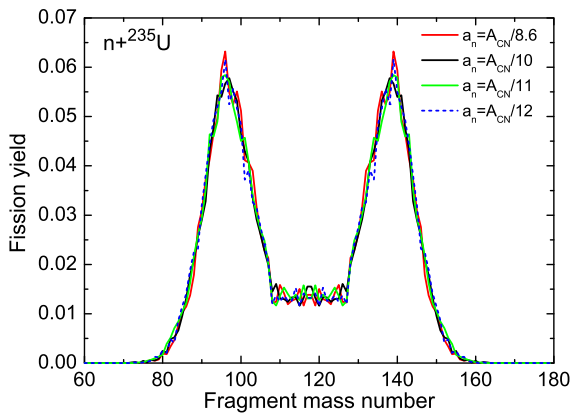

FIG. 4. The fragment mass distributions in 14 MeV $n + {}^{235}$U fission for different values of level density parameters a_n.

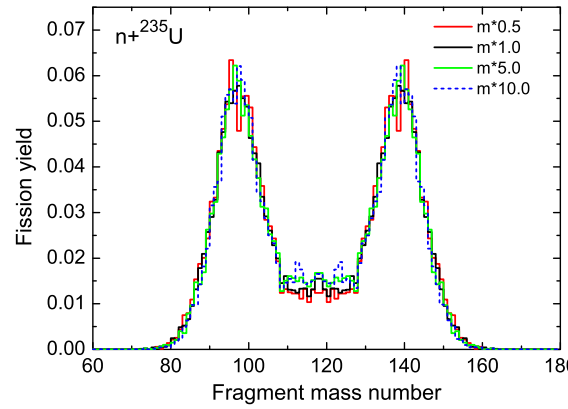

FIG. 6. The fragment mass distributions in 14 MeV $n + {}^{235}$U fission with the inertia tensor multiplied by a factor of 0.5, 1.0, 5.0, and 10.0, respectively.

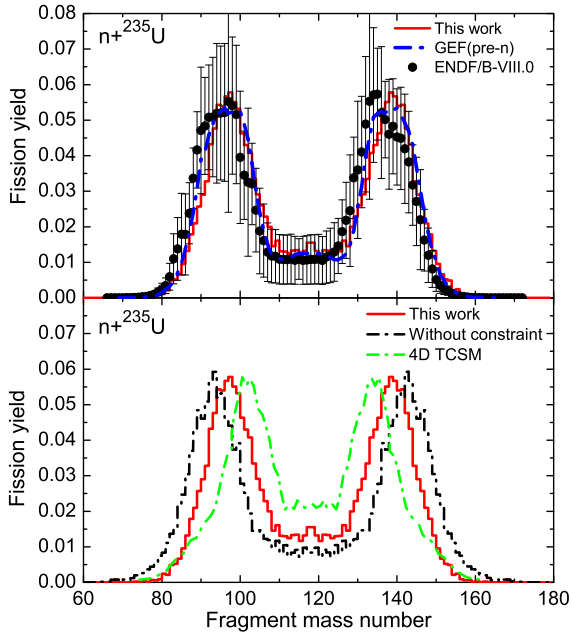

FIG. 7. The calculated fragment mass distribution in 14 MeV $n + {}^{235}$U fission (red line) compared with the preneutron fragment mass distribution calculated with GEF code [42] (blue dash-dot line) and the evaluated data from ENDF/B-VIII.0 [43] (solid circles) (upper panel). The bottom panel shows a comparison between the results of the present work with and without introducing the constraint on the heavy fragment shape (red line and black dash-dot line) and those with a four-dimensional Langevin approach based on the TCSM [24] (green dash-dot line).

Langevin trajectory calculations so as the neutron emission from primary fragments, which will be left for our further studies. Figure 7 shows the fragment mass distribution in 14 MeV $n + {}^{235}$U fission calculated with our model, and the comparisons with the pre-neutron fragment mass distribution calculated with GEF code [42], the evaluated fission yields from ENDF/B-VIII.0 [43] and that with four-dimensional Langevin calculations [24]. It can be seen that there is a good agreement between our model and GEF model calculations for both the peak position and width of fragment mass distribution. The comparison with the results of four-dimensional Langevin calculations also supports the shape constraint on heavy fragments. In the figure, we also show the calculated results without introducing the constraint on the heavy fragment deformation i.e. taking $\delta_1 = \delta_2 = \delta$ in the Langevin trajectory calculation. It sees that the heavy fragment mass distribution shifts to the right side about several mass units while the light fragment mass distribution shifts to the left side a little bit and thus a wider width of whole mass distribution compared with the results of GEF code and the evaluated data. The improvement in the fragment mass distribution by introducing the constraint on the heavy fragment deformation is clearly visible. As for the comparison with the evaluated data from ENDF/B-VIII.0, the overall agreement is also good. The present calculation result is slightly shifted to the right side of mass distribution compared with the evaluated data. It is understandable as we know that the evaluated fission yields

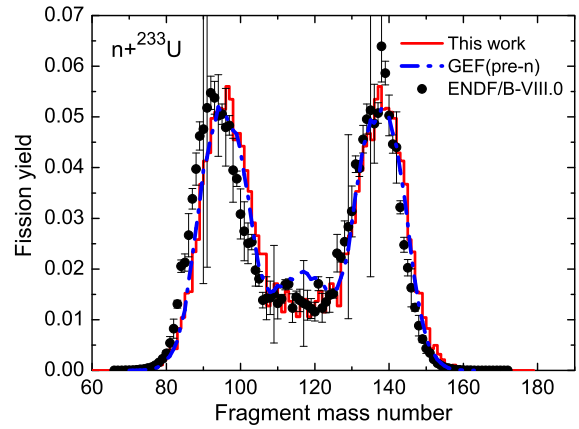

FIG. 8. The calculated fragment mass distribution in 14 MeV $n + {}^{233}$U fission (red curve) compared with the preneutron mass distribution calculated with GEF code [42] (blue dash-dot curve) and the evaluated data from ENDF/B-VIII.0 [43] (solid circles).

are the results of post-neutron fragments, while those of the calculated results are of the primary fragments. And there is a difference of emitted neutron numbers between the primary fragments and the post-neutron fragments. Furthermore, in this work we only calculate the mass distribution from the first chance, which may also influence the results in certain extent.

The calculated fragment mass distributions in 14 MeV $n + {}^{233,238}$U and ^{239}Pu fission are shown in Figs. 8–10, respectively, together with the evaluated data and the results with GEF code. It is shown that the agreement between our calculated results and the results calculated with GEF code as well as the evaluated data shown in Figs. 8–10 is as good as that shown in Fig. 7 and it indicates the rationality and validity of the constraint on the heavy fragment deformation introduced in this work.

In order to study the dependence of the mass distribution on the excitation energies we have also performed the calculations for thermal, 25, 35, 45, and 55 MeV $n + {}^{235}$U fission with the same model parameters. Those results as well as the

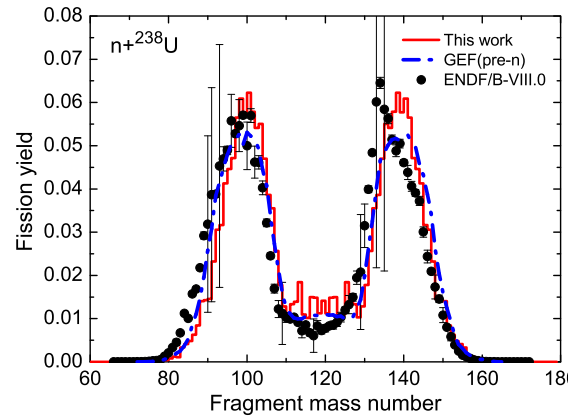

FIG. 9. The calculated fragment mass distribution in 14 MeV $n + {}^{238}$U fission (red curve) compared with the preneutron mass distribution calculated with GEF code [42] (blue dash-dot curve) and the evaluated data from ENDF/B-VIII.0 [43] (solid circles).

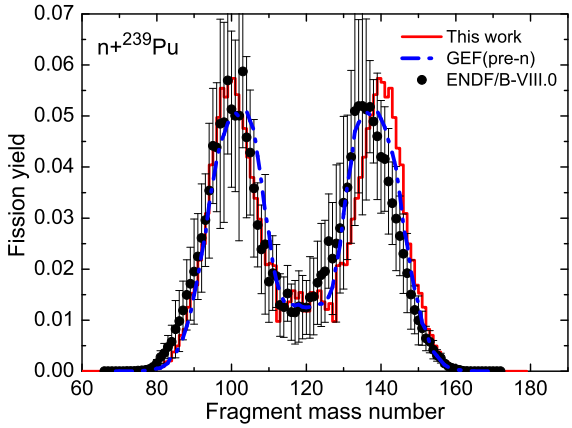

FIG. 10. The calculated fragment mass distribution in 14 MeV $n + {}^{239}$Pu fission (red curve) compared with the preneutron mass distribution calculated with GEF code [42] (blue dash-dot curve) and the evaluated data from ENDF/B-VIII.0 [43] (solid circles).

results at $E_n = 14$ MeV are shown in Fig. 11. It can be found that with the excitation energy increasing, the yields at valley region increase and the yields at peak region decrease with the wider width. Of course, the calculated results can only provide us with the tendency of the dependence of the mass distribution on the excitation energy because multichance fission should be considered as the excitation energy increases; it is not considered here due to the limitation of the model used in the present work.

Another important observable in nuclear fission, the total kinetic energy (TKE) distribution, is also calculated for 14 MeV $n + {}^{235}$U fission. The TKE is the sum of the Coulomb repulsion energy between two fragments and the collective kinetic energy of two fragments along the fission direction at the scission point. Here, the Coulomb interaction between two fragments is simply treated as that between two charged point particles located at the centers of mass of two fragments. Of course, this treatment of the Coulomb energy calculation is a little bit rough but in general it should not change the results too much. The correlation between the total kinetic energy and the heavy fragment mass is shown in Fig. 12,

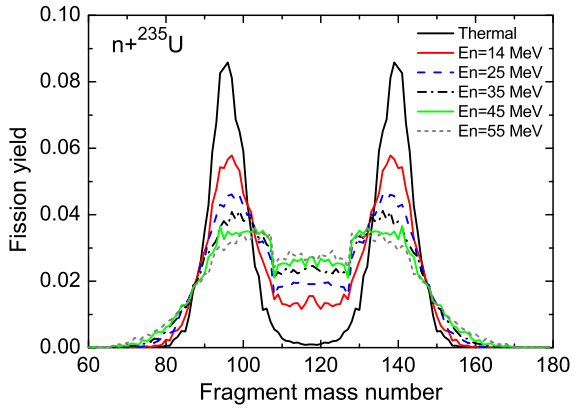

FIG. 11. The calculated fragment mass distribution in $n + {}^{235}$U fission at E_n = thermal, 14, 25, 35, 45, and 55 MeV.

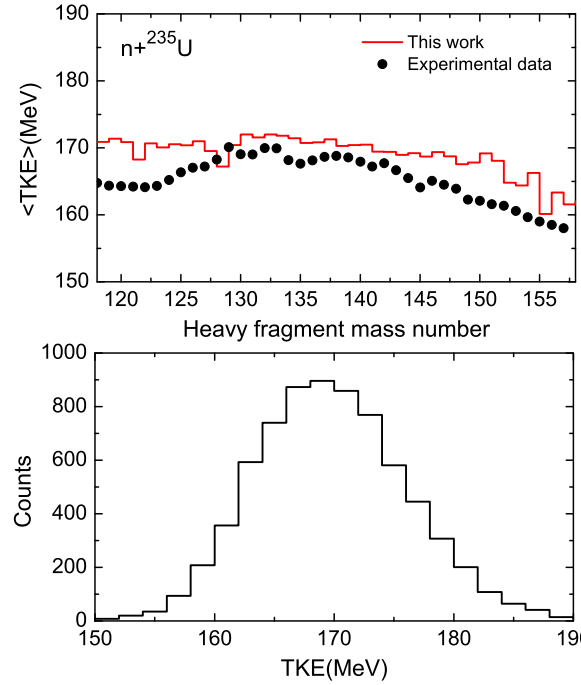

FIG. 12. The correlation of the TKE to the heavy fragment mass number in 14 MeV $n + {}^{235}$U fission and comparison with the experimental data [44] (upper panel). The bottom panel is the distribution of the TKE.

where both calculated results and the experimental data are compared together. In the present work, the calculated TKE is generally larger and flatter compared with the experimental data. In order to find whether the constraint on the shape of heavy fragments causes the TKE distribution at the scission point to be flatter, we have made a comparison of the TKE distribution for cases both with and without constraint. We find that the introduction of the constraint makes the TKE at the mass region around asymmetric fission decrease by about 3 MeV and thus leads to a better agreement with experimental data, but makes no obvious change at the mass region near symmetric fission, which causes the TKE distribution to be flatter. We found that it is because the shape at the heavy fragment side for asymmetric fission becomes more spherical while the elongation of the light fragment side becomes larger compared with the case without constraint. Thus the net effect is to increase the distance between centers of two fragments and eventually to decrease the calculated TKE at the scission point for asymmetric fission around the $N = 82$ shell closure by introduction of the constraint. In order to improve the agreement of the TKE with experimental data, it seems to us that the present model needs further improvement, and a more accurate calculation of the TKE should be performed. The probability distribution of the TKE is also shown in Fig. 12, which is Gaussian type distribution, and the averaged value is about 169 MeV.

C. The fission time

The nuclear fission time is also of importance for understanding the dynamical process of nuclear fission. The fission

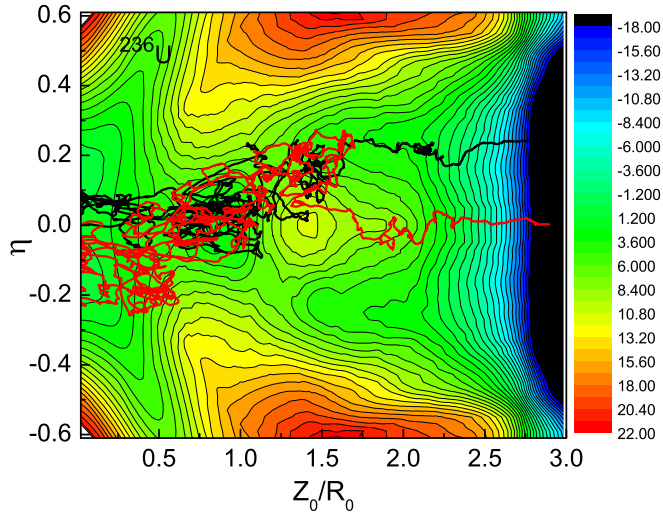

FIG. 13. The potential energy surface for ^{236}U projected on the Z_0/R_0-η plane at $\delta = 0.15$ with ϵ fixed as 0.35. The two Langevin trajectories with the starting position at the ground state are also shown in the figure.

time in this work is defined by the time spent for a Langevin trajectory from the starting point to the scission point. The starting point for the calculation of fission time is taken at the ground state. Figure 13 shows the potential energy surface with $\epsilon = 0.35$ in the Z_0/R_0-η plane at $\delta = 0.15$ for ^{236}U. More intuitively, as an example, in Fig. 13 we also show two Langevin trajectories projected to the Z_0/R_0-η plane. One sees two trajectories with the same starting condition but having different paths: one going to symmetric fission and another to asymmetric fission due to the random force. From Fig. 13 one can find that the two trajectories become parallel to the Z_0/R_0 axis, i.e., the fluctuation of mass asymmetry η, which determines the fragment mass distribution, becomes small when $Z_0/R_0 > 2.5$ (roughly). Then we set the range of the fluctuation in mass asymmetry η to be ± 0.02 and track back all trajectories. We find that as soon as the averaged elongation Z_0 is larger than $2.30R_0$, the fluctuation of η remains $\leqslant 0.02$ for all trajectories. It indicates that the fission fragment mass distribution is formed on the way to reaching the scission point

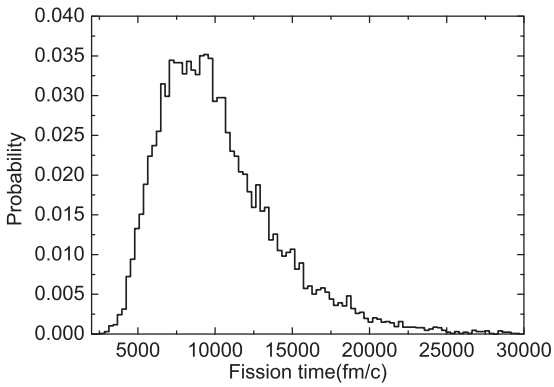

FIG. 14. The fission time distribution in 14 MeV $n + ^{235}$U fission.

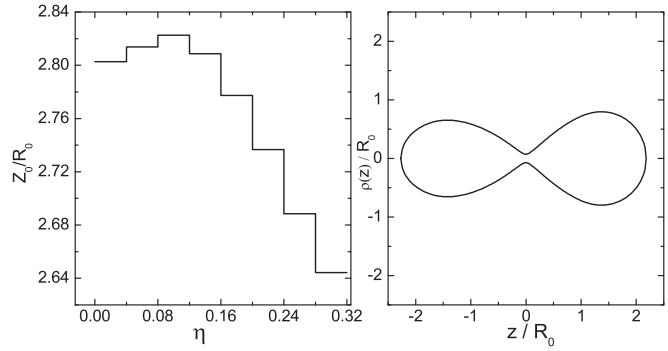

FIG. 15. The correlation of the elongation to the mass asymmetry at the scission point for 14 MeV $n + ^{235}$U fission (left panel) and the averaged nuclear shape at the scission point (right panel).

as the averaged elongation Z_0 at the scission point is about $2.78R_0$.

Figure 14 shows the fission time distribution. One sees that the distribution has a quick increase and slow decrease with a tail of very long fission time, and that the peak is around 8000–10000 fm/c. The uncertainty in the calculation of the fission time mainly comes from the neck size, defined for the scission point based on the model.

The averaged nuclear shape at the scission point is shown in Fig. 15, right panel, where the elongation Z_0 is $2.79R_0$, the mass asymmetry η is 0.16, the deformation parameter δ_L of the light fragment is 0.25, and δ_H is 0.02 for the heavy fragment. It can be seen that the light fragment is more elongated compared with the nearly spherical heavy fragment. It shows from the figure that at the scission point, two fragments are still connected, while in the scission point model, such as that by Pasca *et al.*, the fissioning nucleus at the scission point is modeled by two nearly touching coaxial ellipsoids [45,46]. So the scission point defined in this work is somewhat different from that used in the scission point model. It is more interesting to study the correlation between mass asymmetry and the elongation at the scission point, and

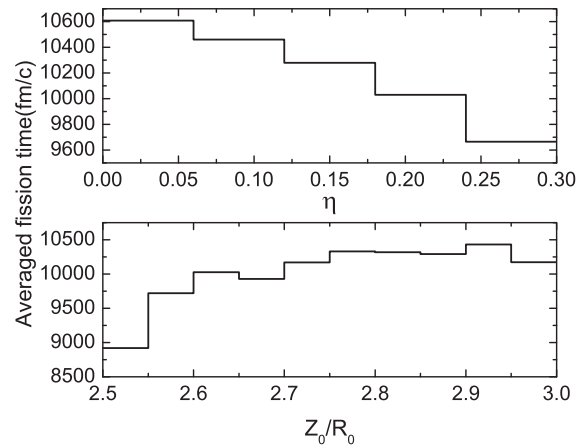

FIG. 16. The correlation of the averaged fission time to mass asymmetry (upper panel) and the elongation (bottom panel) at the scission point for 14 MeV $n + ^{235}$U fission.

the correlation of fission time to mass asymmetry and the elongation for fission events. Figure 15, left panel, shows the correlation between mass asymmetry and the elongation at the scission point, which provides us with information of the scission point configuration. Figure 16 presents the correlation of the averaged fission time to mass asymmetry and the elongation at the scission point. Here in Fig. 16 the averaged fission time means an average over a small range of $\Delta\eta = 0.06$ and $\Delta Z_0/R_0 = 0.05$, respectively. Combining the information obtained from both Figs. 15 and 16 tells us that the symmetric fission is related to a very large elongation and a longer fission time, while the asymmetric fission is related to a smaller elongation and a shorter fission time. This study may shed light on understanding the dynamics of the superlong channel for symmetric fission and the standard channels for asymmetric fission in the GEF model [42] and other phenomenological fission models.

IV. SUMMARY

In this work, we have studied the fission dynamics at low excitation energies based on the three-dimensional Langevin model plus a constraint on the heavy fragment deformation.

We first investigate the influence of the initial condition, the neck radius for setting the scission point, the level density parameter, and the shell damping parameter on the fragment mass distribution. We find that setting the initial conditions to be at the ground state and at the first saddle point has negligible effect, which indicates that the fission yields are mainly determined by the process from the saddle point to the scission point. The neck radius for the scission point setting in the range of 0.0–0.5 fm is reasonable. The influence of the level density parameter is almost invisible, while the shell damping parameter obviously influences the ratio of the yields at peak and valley regions of the fission fragment mass distribution. In addition, the sensitivity of the fragment mass distributions to the values of the inertia tensor for 14 MeV $n + {}^{235}$U fission is also checked, and there is not much obvious influence on the mass distributions.

Then, the fragment mass distributions in 14 MeV $n + {}^{233,235,238}$U and ^{239}Pu fission are calculated and compared with the results of GEF code as well as the evaluated data from ENDF/B-VIII.0, and a very good agreement is obtained. The incorporation of the constraint on the heavy fragment deformation being close to spherical into the three-dimensional Langevin model obviously improves the mass fragment distribution. It seems that the constraint is rational and valid. Moreover, the dependence of the fragment mass distribution on the excitation energy for $n + {}^{235}$U fission is studied within the model, and clearly shows that with the excitation energy increasing, the ratio of the peak to valley decreases and the width of the peak becomes wider. The total kinetic energy distribution correlated with the fragment mass is also calculated for 14 MeV $n + {}^{235}$U fission, and it is more flat compared with the experimental data.

Last, we study the fission time distribution, and it shows a feature of quick increase and slow decrease with a long tail, and the peak of the fission time distribution locates at 8000–10000 fm/c. The correlation between the elongation and mass asymmetry at the scission point as well as the correlation of fission time to the elongation and mass asymmetry at the scission point are studied. The symmetric fission corresponds to a very large elongation and a longer fission time and asymmetric fission corresponds to a smaller elongation and a shorter fission time. It helps us to have a better understanding of the superlong channel for symmetric fission and standard channels for asymmetric fission in the GEF model and other phenomenological models.

Concerning further work, we will incorporate neutron emission into the Langevin equation to make a more realistic study of the fission dynamics.

ACKNOWLEDGMENTS

We would like to thank Prof. J. A. Maruhn for his helpful discussion and suggestion. The work was supported by the National Natural Science Foundation of China under Grants No. 11790324, No. 11790325, No. 11790320, No. 11875125, No. 11475262, No. 11475004, and No. 11675266.

[1] A. Bulgac, P. Magierski, K. J. Roche, and I. Stetcu, Phys. Rev. Lett. **116**, 122504 (2016).
[2] N. Schunck, D. Duke, H. Carr, and A. Knoll, Phys. Rev. C **90**, 054305 (2014).
[3] J. A. Maruhn, P. G. Reinhard, P. D. Stevenson, and A. S. Umar, Comput. Phys. Commun. **185**, 2195 (2014).
[4] J. Randrup and P. Möller, Phys. Rev. Lett. **106**, 132503 (2011).
[5] Y. Aritomo and S. Chiba, Phys. Rev. C **88**, 044614 (2013).
[6] Y. Aritomo, S. Chiba, and F. Ivanyuk, Phys. Rev. C **90**, 054609 (2014).
[7] M. D. Usang, F. A. Ivanyuk, C. Ishizuka, and S. Chiba, Phys. Rev. C **94**, 044602 (2016).
[8] A. J. Sierk, Phys. Rev. C **96**, 034603 (2017).
[9] M. D. Usang, F. A. Ivanyuk, C. Ishizuka, and S. Chiba, Phys. Rev. C **96**, 064617 (2017).
[10] M. R. Pahlavani and S. M. Mirfathi, Phys. Rev. C **92**, 024622 (2015).
[11] T. Asano, T. Wada, M. Ohta, T. Ichikawa, S. Yamaji, and H. Nakahara, J. Nucl. Radiochem. Sci. **5**, 1 (2004).
[12] P. Möller, D. G. Madland, A. J. Sierk, and A. Iwamoto, Nature (London) **409**, 785 (2001).
[13] P. Möller, A. J. Sierk, T. Ichikawa, A. Iwamoto, R. Bengtsson, H. Uhrenholt, and S. Åberg, Phys. Rev. C **79**, 064304 (2009).
[14] K. Pomorski and J. Dudek, Phys. Rev. C **67**, 044316 (2003).
[15] J. Randrup, P. Möller, and A. J. Sierk, Phys. Rev. C **84**, 034613 (2011).
[16] K. Pomorski, F. A. Ivanyuk, and B. Nerlo-Pomorska, Eur. Phys. J. A **53**, 59 (2017).
[17] Y. Abe, S. Ayik, P.-G. Reinhard, and E. Suraud, Phys. Rep. **275**, 49 (1996).
[18] P. Fröbrich and L. I. Gontchar, Phys. Rep. **292**, 131 (1998).

[19] T. Wada, Y. Abe, and N. Carjan, Phys. Rev. Lett. **70**, 3538 (1993).
[20] J. Bao, Y. Zhuo, and X. Wu, Z. Phys. A **352**, 321 (1995).
[21] A. V. Karpov, P. N. Nadtochy, D. V. Vanin, and G. D. Adeev, Phys. Rev. C **63**, 054610 (2001).
[22] Y. Abe, C. W. Shen, G. I. Kosenko, and D. Boilley, Phys. At. Nucl. **66**, 1057 (2003).
[23] G. D. Adeev, A. V. Karpov, P. N. Nadtochii, and D. V. Vanin, Fiz. Elem. Chastits At. Yadra **36**, 712 (2005) [Phys. Part. Nucl. **36**, 378 (2005)].
[24] C. Ishizuka, M. D. Usang, F. A. Ivanyuk, J. A. Maruhn, K. Nishio, and S. Chiba, Phys. Rev. C **96**, 064616 (2017).
[25] M. T. S. Kannan, J. Sadhukhan, B. K. Agrawal, M. Balasubramaniam, and S. Pal, Phys. Rev. C **98**, 021601(R) (2018).
[26] J. A. Maruhn and W. Greiner, Z. Phys. **251**, 431 (1972).
[27] K. T. R. Davies, A. J. Sierk, and J. R. Nix, Phys. Rev. C **13**, 2385 (1976).
[28] J. Blocki, Y. Boneh, J. R. Nix, J. Randrup, M. Robel, A. J. Sierk, and W. J. Swiatecki, Ann. Phys. (NY) **113**, 330 (1978).
[29] H. Feldmeier, Rep. Prog. Phys. **50**, 915 (1987).
[30] H. J. Krappe, J. R. Nix, and A. J. Sierk, Phys. Rev. C **20**, 992 (1979).
[31] A. J. Sierk, Phys. Rev. C **33**, 2039 (1986).
[32] V. M. Strutinsky, Nucl. Phys. A **95**, 420 (1967).
[33] M. Brack, J. Damgaard, A. S. Jensen, H. C. Pauli, V. M. Strutinsky, and C. Y. Wong, Rev. Mod. Phys. **44**, 320 (1972).
[34] S. G. Nilsson, C. F. Tsang, A. Sobiczewski, Z. Szymański, S. Wycech, C. Gustafson, I.-L. Lamm, P. Möller, and B. Nilsson, Nucl. Phys. A **131**, 1 (1969).
[35] A. V. Ignatyuk, K. K. Istekov, and G. N. Smirenkin, Yad. Fiz. **29**, 895 (1979) [Sov. J. Nucl. Phys. **29**, 450 (1979)].
[36] S. Yamaji, H. Hofmann, and R. Samhammer, Nucl. Phys. A **475**, 487 (1987).
[37] H. Hofmann and D. Kiderlen, Int. J. Mod. Phys. E **07**, 243 (1998).
[38] P. N. Nadtochy, E. G. Ryabov, A. E. Gegechkori, Yu. A. Anischenko, and G. D. Adeev, Phys. Rev. C **85**, 064619 (2012).
[39] A. V. Karpov and V. V. Saiko, Phys. Rev. C **96**, 024618 (2017).
[40] H. J. Krappe and K. Pomorski, *Theory of Nuclear Fission: A Textbook*, Lecture Notes in Physics Vol. 838 (Springer, Berlin, 2012).
[41] J. R. Nix and A. J. Sierk, Nucl. Phys. A **428**, 161 (1984).
[42] K.-H. Schmidt, B. Jurado, C. Amouroux, and C. Schmitt, Nucl. Data Sheets **131**, 107 (2016).
[43] D. A. Brown *et al.*, Nucl. Data Sheets **148**, 1 (2018).
[44] P. P. Dyachenko, B. D. Kuzminov, and M. Z. Tarasko, Sov. J. Nucl. Phys. **8**, 165 (1969).
[45] H. Pasca, A. V. Andreev, G. G. Adamian, N. V. Antonenko, and Y. Kim, Phys. Rev. C **93**, 054602 (2016).
[46] H. Pasca, A. V. Andreev, G. G. Adamian, and N. V. Antonenko, Nucl. Phys. A **969**, 226 (2018).